

Earth and Space Science



RESEARCH ARTICLE

10.1029/2023EA003136

Key Points:

- Weather Research and Forecasting (WRF)-enhanced Precise Point Positioning (PPP) strategies improve positioning accuracy in the up component for both static and kinematic modes
- WRF-enhanced PPP strategies accelerate static positioning convergence speed in the up component
- WRF-enhanced PPP strategies show a larger positioning accuracy improvement in wet period

Correspondence to:

Z. Liu,
lszzliu@polyu.edu.hk

Citation:

Gong, Y., Liu, Z., Yu, S., Chan, P. W., & Hon, K. K. (2024). Improving GNSS PPP performance in the South China under different weather conditions by using the Weather Research and Forecasting (WRF) model-derived wet delay corrections. *Earth and Space Science*, 11, e2023EA003136. <https://doi.org/10.1029/2023EA003136>

Received 9 SEP 2023
Accepted 24 JAN 2024

Author Contributions:

Conceptualization: Zhizhao Liu
Data curation: Pak Wai Chan, Kai Kwong Hon
Formal analysis: Yangzhao Gong, Zhizhao Liu, Shiwei Yu
Funding acquisition: Zhizhao Liu
Investigation: Yangzhao Gong
Methodology: Yangzhao Gong
Project administration: Zhizhao Liu
Software: Yangzhao Gong, Shiwei Yu
Supervision: Zhizhao Liu
Validation: Yangzhao Gong
Writing – original draft: Yangzhao Gong
Writing – review & editing: Zhizhao Liu

© 2024 The Authors. Earth and Space Science published by Wiley Periodicals LLC on behalf of American Geophysical Union.

This is an open access article under the terms of the [Creative Commons Attribution-NonCommercial-NoDerivs License](https://creativecommons.org/licenses/by/4.0/), which permits use and distribution in any medium, provided the original work is properly cited, the use is non-commercial and no modifications or adaptations are made.

Improving GNSS PPP Performance in the South China Under Different Weather Conditions by Using the Weather Research and Forecasting (WRF) Model-Derived Wet Delay Corrections

Yangzhao Gong¹, Zhizhao Liu¹ , Shiwei Yu¹ , Pak Wai Chan² , and Kai Kwong Hon² 

¹Department of Land Surveying and Geo-Informatics, The Hong Kong Polytechnic University, Kowloon, China, ²Hong Kong Observatory, Kowloon, China

Abstract Atmospheric wet delay caused by Precipitable Water Vapor (PWV) significantly impacts the performance of many geodetic surveying systems such as Global Navigation Satellite System (GNSS). In this study, we use wet delay corrections forecast by the Weather Research and Forecasting (WRF) model to enhance GNSS Precise Point Positioning (PPP) during two observation periods with two different weather conditions, that is, period 1: March 01 to 14, 2020 (average PWV: 23.5 kg/m²) and period 2: June 02 to 15, 2020 (flooding weather with average PWV: 55.6 kg/m²), over the South China. PWV data from 277 to 263 GNSS stations are assimilated into WRF model to enhance the WRF water vapor forecasting capability for period 1 and period 2, respectively. Wet delay corrections from two different WRF configurations, that is, WRF no data assimilation and WRF with assimilation of GNSS PWV, are used to augment the PPP. Totally, eight WRF-enhanced PPP schemes are tested. The results show that WRF-enhanced PPP schemes generally have a better positioning performance in the up component than traditional PPP. After using WRF wet delay corrections, for static mode, the vertical positioning accuracy is improved by 14.6% and 33.7% for period 1 and period 2, respectively. The corresponding convergence time are reduced by 41.8% and 25.0% for period 1 and period 2, respectively. For kinematic mode, the positioning accuracy improvements in the up component reach 13.8% and 19.0% for period 1 and period 2, respectively. The kinematic PPP convergence time is reduced by up to 8.2% for period 1.

Plain Language Summary Global Navigation Satellite System (GNSS) signal is significantly delayed by the water vapor in the Earth's troposphere. How to mitigate this so-called wet delay has long been a challenging problem in GNSS Precise Point Positioning (PPP) community. In this study, we use the Weather Research and Forecasting (WRF) model to simulate the distribution and variation of water vapor over the South China during two periods with different water vapor conditions, that is, period 1: March 01 to 14, 2020 (average PWV: 23.5 kg/m²) and period 2: June 02 to 15, 2020 (flooding weather with average PWV: 55.6 kg/m²). In addition, water vapor data from 277 and 263 GNSS stations have been assimilated into the WRF model for period 1 and period 2, respectively, to further improve WRF water vapor forecasting accuracy. The high-quality water vapor forecasts are then used to correct the wet delay for GNSS PPP. Our results show that, with use of the wet delay corrections forecast by the WRF model, GNSS PPP can achieve a better performance in positioning accuracy and convergence speed during both two periods.

1. Introduction

Atmospheric wet delay caused by Precipitable Water Vapor (PWV) is one of major error budgets in Global Navigation Satellite System (GNSS), particularly in GNSS Precise Point Positioning (PPP) where no cancellation between two stations is possible. The value of Zenith Wet Delay (ZWD) in the humid areas can reach 0.4 m (Businger et al., 1996), which significantly degrades the GNSS PPP positioning accuracy, particularly in the vertical component (Wang & Liu, 2019; Zhou et al., 2020). In GNSS traditional PPP, the atmospheric wet delay is normally treated as an unknown parameter to be estimated together with the coordinates by using the Kalman filter or least squares method (Kouba & Héroux, 2001; Zumberge et al., 1997). However, this PPP processing strategy normally needs a relatively long time, for example, more than 30 min, to converge to an accuracy of sub-decimeter level in the vertical component using single-constellation observations (Wang & Liu, 2019). Accurate and reliable external water vapor correction information is therefore crucial for GNSS PPP.

The Weather Research and Forecasting (WRF) model (Skamarock et al., 2019) is a mesoscale Numerical Weather Prediction (NWP) model that can forecast the three-dimensional (3D) distribution of humidity, temperature, and pressure, with a high spatiotemporal resolution, for example, a few kilometers of spatial resolution and hourly temporal resolution. Several studies have demonstrated the good performance of WRF model in water vapor forecasting (Leontiev et al., 2020; Mateus et al., 2015). For example, using 6 years of radiosonde data in Lisbon region as the reference, Mateus et al. (2015) concluded that the mean standard deviation of WRF-derived wet delay was 4.46 mm. Some previous studies also have proven that assimilation of external water vapor data, for example, GNSS PWV and Interferometric synthetic aperture radar (InSAR) PWV, into the WRF model can improve the WRF model's performance in forecasting PWV (Leontiev et al., 2020; Mateus & Miranda, 2022; Mateus et al., 2021; Xiong et al., 2020). For example, Leontiev et al. (2020) assimilated PWV data from the Global Positioning System (GPS) PWV maps augmented by the Meteosat satellite imagery data into the WRF model to improve its PWV forecasting accuracy in Israel and neighboring areas. Their results indicated that the WRF model can forecast PWV with a root mean square error (RMSE) of 2.5–2.6 kg/m² for the forecast length of 3–12 hr. After assimilating GPS PWV map combined with Meteosat satellite data, the corresponding RMSE values were reduced to around 1.8 kg/m².

In recent years, many studies have adopted WRF model to correct atmospheric delay in geodetic surveying, such as InSAR surveying (Dou et al., 2021; Murray et al., 2019; Wang et al., 2021; Webb et al., 2020). However, very little work has studied WRF-derived atmospheric delay to augment GNSS PPP (Gong et al., 2021; Vaclavovic et al., 2017; Wilgan et al., 2017). Wilgan et al. (2017) combined the tropospheric Zenith Total Delay (ZTD) from a local GNSS network and a high spatial resolution (4 km × 4 km) WRF model by using a least-squares collocation software COMEDIE (Collocation of Meteorological Data for Interpretation and Estimation of Tropospheric Path delays) to generate a local GNSS/WRF ZTD model in Poland and adjacent areas. The GNSS/WRF ZTD corrections were then used to augment GNSS PPP. Observations from 14 GNSS stations for 3 weeks with three different tropospheric conditions were used in their PPP experiments. Their results reported that, compared with traditional PPP solution, GNSS/WRF-based ZTD enhanced PPP schemes can reduce convergence time from 67 to 58 min for the horizontal component and from 79 to 63 min for the up component, when using 0.1 m as the convergence threshold for both horizontal and up components. Gong et al. (2021) performed six consecutive 24-hr WRF runs (from April 06 to 11, 2020) to model the water vapor over the South China. GNSS PWV data and radiosonde profiles were assimilated into the WRF model to improve the water vapor forecasting performance. The results indicated that GNSS PPP positioning accuracy and convergence speed can be improved after using WRF-derived wet delay corrections to fix GNSS PPP wet delay parameter.

However, there are still some limitations in previous studies. First, the amount of external water vapor data (water vapor data from 27 GNSS stations and meteorological profiles from 22 radiosonde stations) assimilated into the WRF model is insufficient (Gong et al., 2021). Second, the accuracy of PWV derived from WRF model after data assimilation and their efficiency in augmenting GNSS positioning during wet weather conditions have not been comprehensively studied. Investigating the performance of WRF-enhanced PPP under different weather conditions is thus needed.

In this study, we performed 28 full-day (24-hr) forecasts for the South China region for two periods, that is, period 1: March 01 to 14, 2020 and period 2: June 02 to 15, 2020, to investigate the performance of GNSS PPP after being enhanced by WRF-derived wet delay corrections under different weather conditions. It should be noted that the South China region including the Yangtze basin experienced a flooding weather condition during 2020 summer season (Guo et al., 2020). In this study, to enhance the accuracy of WRF-derived wet delay corrections, PWV observations from 277 and 263 GNSS stations are assimilated into WRF model in period 1 and period 2, respectively. The WRF-derived wet delay corrections are used to enhance GNSS PPP in two different ways. One way is to use WRF-derived wet delay corrections to directly fix the wet delay parameter in GNSS PPP directly while the other way is to treat WRF-derived wet delay corrections as pseudo observations of wet delay and constrain the wet delay parameter in GNSS PPP estimation. The impact of different augmentation strategies on GNSS PPP performance is analyzed comprehensively in this study.

The remaining part of paper is organized as follows. First, the configurations of WRF data assimilation experiment and the WRF PWV and wet delay correction retrieval methods will be introduced in Section 2. The water vapor conditions for the two periods and the accuracy of WRF water vapor forecasting accuracy will be analyzed in Section 3. The data and processing strategies adopted in the GNSS PPP study are described in Section 4.

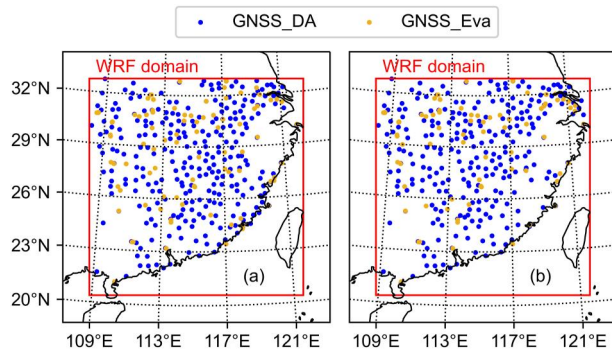


Figure 1. The distributions of WRF domain, GNSS assimilation stations (GNSS_DA), and GNSS evaluation stations (GNSS_Eva) for (a) period 1 (March 01 to 14, 2020), and (b) period 2 (June 02 to 15, 2020).

Section 5 presents the PPP positioning results and the related analyses. Section 6 discusses the WRF-enhanced PPP positioning results and the value of this study. Finally, the conclusions are given in Section 7.

2. Description of WRF Water Vapor Data

2.1. WRF Model Configurations

The WRF model in this study is configured with Advanced Research WRF (ARW) core version 4.2 (Skamarock et al., 2019). A single WRF domain with 280 grid points in the west-east dimension and 283 grid points in the south-north dimension is adopted to cover the main part of South China, as shown in Figure 1. The horizontal spatial resolution of WRF domain is 5 km for both west-east and south-north dimensions. For the vertical dimension, 36 vertical levels are set. The European Centre for Medium-Range Weather Forecasts (ECMWF) Reanalysis v5 (ERA5) hourly reanalysis data (Hersbach et al., 2020) with a spatial resolution of 0.25° are used as the WRF initial and

boundary conditions. In addition, the main physics-related model options adopted in the WRF model are listed as follows. WRF double moment 6-class scheme (Lim & Hong, 2010) is adopted for micro physics option. Rapid Radiative Transfer Model for General Circulation Models (RRTMG) shortwave and longwave schemes (Iacono et al., 2008) are selected for shortwave and longwave radiation options, respectively. Kain-Fritsch scheme (Kain, 2004) is applied for cumulus parameterization. 5-layer thermal diffusion scheme (Dudhia, 1996) is selected for land surface option. Yonsei University scheme (Hong et al., 2006) is selected for the planetary boundary layer physics option. The WRF domain size and the selection of physical options are similar with other WRF experiments conducted by the operational weather prediction center over the South China area (Chan et al., 2022; Hon, 2020).

We totally perform 28 full-day (24-hr) WRF runs over the South China for two periods, that is, period 1 (March 01 to 14, 2020) and period 2 (June 02 to 15, 2020). All 24-hr WRF runs in this study are initialized at 0 hr UTC for each day and the meteorological parameters including water vapor mixing ratio, air pressure, and air temperature, are forecast hourly for the following 24 hr.

2.2. Assimilation of GNSS PWV Into WRF Model

The WRF data assimilation system embedded in the WRF framework can assimilate external meteorological observations to enhance the WRF initial field and further improve the forecasting performance. In this study, to investigate the impact of assimilating GNSS PWV, two WRF configurations, that is, WRF configuration 0 (no data assimilation) and WRF configuration 1 (with assimilation of GNSS PWV), are adopted. For WRF 1, WRF three-dimensional variational (3DVAR) assimilation method (Barker et al., 2004) is applied to assimilate GNSS PWV observations at 0 hr UTC of each day (WRF initialization time). 3DVAR is an effective assimilation method that can assimilate external meteorological observations to update the initial field of the WRF model. The optimal initial field is estimated by minimizing the 3DVAR cost function, which is shown below (Barker et al., 2004):

$$J(x) = \frac{1}{2}(x - x_b)^T B^{-1}(x - x_b) + \frac{1}{2}(y - H(x))^T R^{-1}(y - H(x)) \quad (1)$$

where $J(x)$ is the scalar cost function; x stands for the WRF meteorological analysis field; x_b is the WRF background field. In this study, y represents the GNSS PWV observations assimilated; $H(x)$ is the PWV operator; B is the covariance matrix of background errors; R is the covariance matrix of observation errors. In this study, the control variables option 5 (CV5) background error covariance calculated by the National Meteorological Centre (NMC) method (Parrish & Derber, 1992) is used. The NMC method determines the background error covariance based on the difference between WRF forecasting results at forecast lengths 24 and 12 hr over a month (March 2020 for experiment period 1 and June 2020 for experiment period 2 in this study). Additionally, observation error 2 kg/m² is assigned to GNSS PWV according to the accuracy specification of GNSS PWV data assimilated. The details of GNSS PWV assimilated have been introduced as below.

Two GNSS PWV data sets, that is, the China Meteorological Administration GNSS Network (CMAGN) water vapor products and the Crustal Movement Observation Network of China (CMONOC) tropospheric delay products, are used in this study. For period 1 and period 2, 370 and 342 GNSS stations are used, respectively. Specifically, for period 1, PWV from 277 GNSS stations are assimilated into the WRF model, and the remaining 93 GNSS stations are used to assess the WRF PWV forecasting accuracy; for period 2, there are 263 GNSS stations used for assimilation and 79 GNSS stations used for evaluation. Liang et al. (2015) reported that, GNSS PWV from CMAGN and CMONOC water vapor products have a difference of around 2 kg/m² in comparison with radiosonde PWV. The GNSS PWV data accuracy of 2 kg/m² is well better than the WRF PWV forecasting accuracy in this study so they can be used as a reference of the true PWV.

The distribution of GNSS assimilation stations and evaluation stations for period 1 and period 2 are shown in Figures 1a and 1b, respectively. Basically, the GNSS assimilation stations and evaluation stations have an even distribution.

2.3. Retrieval Method of WRF PWV and Wet Delay

Using WRF meteorological outputs, for example, water vapor mixing ratio, air pressure, air temperature, the WRF PWV and wet delay can be calculated as follows. PWV (unit: kg/m²) can be calculated by integrating the specific humidity q (unit: kg/kg) with respect to the air pressure P (unit: hPa) (Ross & Elliott, 1996):

$$PWV = \frac{1}{g} \int_{P_{top}}^{P_s} q dP \times 100 \quad (2)$$

where g represents the gravitational acceleration constant (9.81 m/s²). q is the specific humidity that can be calculated using WRF water vapor mixing ratio Q (unit: kg/kg) forecasts:

$$q = \frac{Q}{Q + 1} \quad (3)$$

ZWD (unit: m) can be calculated as an integration of atmosphere wet refractivity N_w (unitless) with respect to height h (unit: m) (Askne & Nordius, 1987):

$$ZWD = 10^{-6} \int N_w dh \quad (4)$$

Wet refractivity can be calculated using (Askne & Nordius, 1987):

$$N_w = \left(k_2 - k_1 \frac{R_d}{R_w} \right) \frac{e}{T} + k_3 \frac{e}{T^2} \quad (5)$$

where k_1 , k_2 , and k_3 are three empirical refractivity constants. In this study, the “best average” values: $k_1 = 77.6890$ K/hPa, $k_2 = 71.2952$ K/hPa, $k_3 = 375,463$ K²/hPa calculated by Rieger (2002) are adopted. R_d (287.053 J/K/kg) is the gas constant for dry air and R_w (461.495 J/K/kg) is the gas constant for water vapor. T (unit: K) is air temperature from WRF. Water vapor partial pressure e (unit: hPa) can be calculated based on WRF water vapor mixing ratio Q (unit: kg/kg) and WRF air pressure P (unit: hPa):

$$e = \frac{Q \cdot P}{0.622 + Q} \quad (6)$$

3. Analyses of Water Vapor Conditions and WRF Water Vapor Forecasting Accuracy

3.1. Water Vapor Conditions During Two Experiment Periods

The GNSS average PWV at each GNSS station for period 1 and period 2 are shown in Figures 2a and 2b, respectively. Generally, GNSS stations with lower latitudes have larger PWV values. The PWV values in period 1 are much lower than those in period 2. Specifically, the overall GNSS average PWV for period 1 and period 2 are

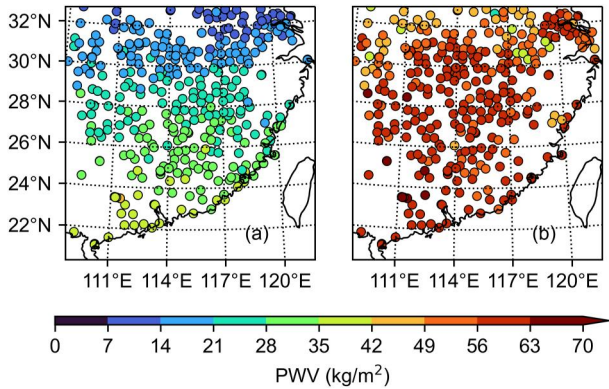


Figure 2. GNSS average PWV for each GNSS station (including both GNSS assimilation station and GNSS evaluation station) for (a) period 1 (March 01 to 14, 2020) and (b) period 2 (June 02 to 15, 2020).

23.5 and 55.6 kg/m², respectively. Additionally, the PWV standard deviation of each GNSS station for each period is calculated, the overall PWV average standard deviation for period 1 and period 2 are 6.6 and 8.7 kg/m², respectively.

3.2. WRF Water Vapor Forecasting Accuracy

Before using WRF water vapor corrections to improve GNSS PPP performance, it is necessary to have clear knowledge about the WRF water vapor forecasting accuracy. We have conducted the WRF PWV RMSE statistics at the initialization time and the following 24 forecasting (forecast length from 1 to 24 hr) for both WRF configuration 0 (no data assimilation) and WRF configuration 1 (assimilation of GNSS PWV). The RMSE of WRF PWV evaluated by independent GNSS PWV for period 1 and period 2 are shown in Figures 3a and 3b, respectively. The independent GNSS PWV data are used for evaluation only and have not been assimilated into the WRF model. The WRF PWV are compared with collocated GNSS PWV and their differences

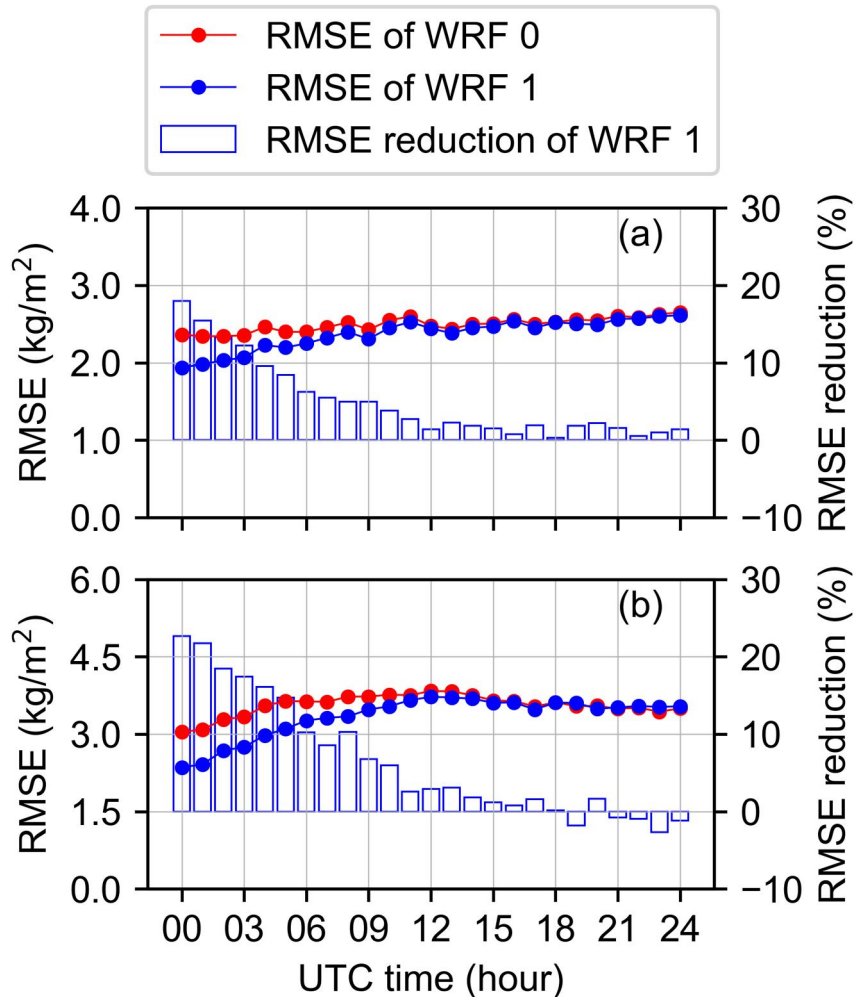


Figure 3. The RMSE of WRF PWV evaluated by GNSS PWV for (a) period 1 (March 01 to 14, 2020); and (b) period 2 (June 02 to 15, 2020). The bar represents the percentage of RMSE reduction of WRF configuration 1 (assimilation of GNSS PWV) compared with WRF configuration 0 (no data assimilation). GNSS PWV used in evaluation have not been assimilated into WRF model. For WRF configuration 1, the GNSS PWV are assimilated into WRF model at 0 hr UTC of each day during period 1 and period 2.

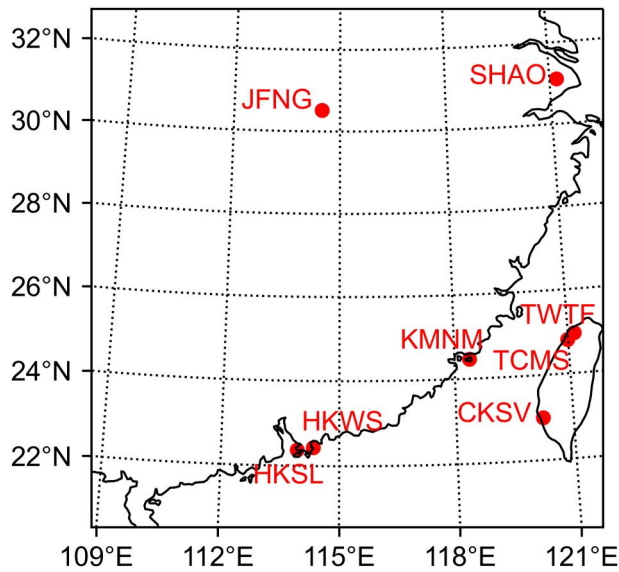


Figure 4. The geographical distribution of eight IGS stations used for GNSS PPP.

are calculated. The WRF PWV data are considered as outliers and removed in the RMSE statistics if the differences are over 12 kg/m^2 . We can see that the WRF PWV RMSE for period 1 are evidently smaller than that for period 2. The two WRF configurations for period 1 have the PWV RMSE ranging from around 1.9 to 2.7 kg/m^2 , while the PWV RMSE of two WRF configurations for period 2 range from around 2.4 to 3.8 kg/m^2 .

We can clearly see that assimilation of GNSS PWV evidently reduces the WRF PWV forecasting RMSE. Compared with WRF configuration 0, WRF configuration 1 has a smaller RMSE in all the 24 hr forecast lengths in period 1. In period 2, WRF configuration 1 can reduce the RMSE in almost all the 24 hr forecast lengths. The positive effect of assimilating GNSS PWV decreases when the forecast length increases. Compared to WRF configuration 0, the RMSE of WRF configuration 1 has reduced by 18.0% at the data assimilation time (0 UTC) but the RMSE reduction becomes 1.4% at 12 hr forecast length (12 UTC). For period 2, WRF configuration 1 has a reduction of 22.6% at 0 UTC. This reduction decreases to 2.9% when the forecast length increases to 12 hr. For both period 1 and period 2, as well as both two WRF configurations, we can see that the WRF PWV forecasting accuracy evidently degrades when the forecast length increases, particularly in the first 12 hr.

4. Description of GNSS PPP Experiment

4.1. GNSS Data Used in GNSS PPP

WRF-derived wet delay corrections are used to improve GNSS PPP performance for two periods with two different weather conditions, that is, period 1 (March 01 to 14, 2020, average PWV: 23.5 kg/m^2) and period 2 (June 02 to 15, 2020, flooding weather with average PWV: 55.6 kg/m^2). GNSS observations from eight International GNSS Service (IGS) GNSS stations with a sampling rate of 30 s are adopted for PPP experiment during these two periods. The geographic distribution of eight GNSS stations is shown in Figure 4. Only GPS observations are used in this study. It should be noted that the observations for station TCMS on March 01, June 05 to 06, 2020 are missing. The observations for KMNM on March 09, 2020 and observations for HKWS on June 07, 2020 are also absent.

4.2. GNSS PPP Positioning Strategies

We totally tested nine different GNSS PPP schemes including a traditional PPP scheme and eight WRF-enhanced PPP schemes in both static and kinematic modes for both periods, as shown in Table 1. The only difference between traditional PPP scheme and WRF-enhanced PPP schemes is the atmospheric wet delay processing strategy.

Table 1
Tropospheric Wet Delay Processing Strategies for Nine Different GNSS PPP Schemes Adopted in This Study

PPP schemes	Tropospheric wet delay parameter processing strategies	Constraint value set
Traditional	Estimated as an unknown parameter	–
WRF 0_F	Fixed by wet delay corrections from WRF configuration 0	–
WRF 0_C_15 mm	Estimated as an unknown parameter and constrained by wet delay corrections from WRF configuration 0	15 mm
WRF 0_C_20 mm		20 mm
WRF 0_C_25 mm		25 mm
WRF 1_F	Fixed by wet delay corrections from WRF configuration 1	–
WRF 1_C_15 mm	Estimated as an unknown parameter and constrained by wet delay corrections from WRF configuration 1	15 mm
WRF 1_C_20 mm		20 mm
WRF 1_C_25 mm		25 mm

In the traditional PPP scheme, the wet delay is estimated as random walk process with a spectral density of $3 \times 10^{-8} \text{ m}^2/\text{s}$. In WRF-enhanced PPP schemes, the first step is to obtain the WRF-derived wet delay corrections. The WRF forecasting is conducted hourly at each UTC hour. In this work, WRF-derived wet delay corrections between two UTC hours are linearly interpolated at an interval of 30 s, same as the GNSS data interval in this study. Then in the WRF-enhanced GNSS PPP, the interpolated WRF-derived wet delay corrections are used in two schemes: one is to fix the WRF wet delay correction as wet delay parameter in PPP, called WRF-fixed PPP; the other is to treat WRF wet delay corrections as pseudo observations to constrain the wet delay parameter in GNSS PPP, which is called WRF-constrained PPP.

For WRF-constrained PPP, it is important to assign a reasonable constraint to the WRF-derived wet delay “observations.” In this study, three different constant constraint values, that is, 15, 20, and 25 mm, are adopted. The selection of these values is based on the WRF PWV evaluation results shown in Figure 3. The WRF PWV forecasting accuracies for WRF configuration 0 (no data assimilation) and WRF configuration 1 (with assimilation of GNSS PWV) are basically within 1.9–3.8 kg/m² in both period 1 and period 2. Considering the ratio value of PWV/ZWD is approximately 0.15 (Bevis et al., 1994), the constraints of 15–25 mm for ZWD are estimated.

Other common PPP processing strategies are summarized as follows. Observation errors of 0.3 and 0.003 m are assigned to GNSS pseudorange and carrier phase observations, respectively. The observation weight is determined by the elevation-dependent weighting scheme. The observation cut-off elevation angle is set to 10°. Ionosphere-free combination is adopted to eliminate the ionospheric delay. Satellite clock and orbit are fixed by IGS final satellite clock products and IGS final orbit products, respectively. The tropospheric hydrostatic delay corrections are calculated using the Saastamoinen model (Davis et al., 1985; Saastamoinen, 1972). The pressure at GNSS station used in Saastamoinen model can be calculated using the pressure reduction method proposed by Hopfield (1969) based on ERA5 surface pressure and 2 m temperature data. For GNSS static PPP mode, the station coordinates are estimated as constants; for kinematic PPP mode, the coordinates are estimated as random walk with spectral density of $10^4 \text{ m}^2/\text{s}$. The reference coordinates used to evaluate for PPP results are extracted from IGS daily station position file. For the station SHAO, daily static PPP positioning results calculated by the Canadian Spatial Reference System (CSRS)-PPP online software (Tétreault et al., 2005) are used as reference coordinates since IGS has no coordinate solution for this station during experiment periods.

It should be noted that only GNSS observations and WRF-derived wet delay corrections within the first 6 hr of each day (0–6 UTC) are used for PPP processing in both period 1 and period 2 in this study. This is because of considering two facts: (a) the effectiveness of GNSS PWV assimilation into WRF decreases when forecast length increases; (b) the accuracy of WRF-derived wet delay corrections degrades when forecast length increases.

5. PPP Positioning Results and Analyses

5.1. PPP Positioning Errors at Early Positioning Stage

For each GNSS station, the daily GNSS data (actually the first 6 hr of observations for each day) in both period 1 and period 2 are processed in PPP mode using all the nine schemes to treat the wet delay. The PPP results of each set of GNSS data (each station, each day, and each scheme) in the first 30 min of positioning time are evenly divided into six 5-min groups according to their positioning time range of 0–5 min, 5–10 min, 10–15 min, 15–20 min, 20–25 min, and 25–30 min. The positioning RMSE of each set of PPP solution (each station, each day, each PPP scheme, each 5-min group, and each component as well as 3D position) is calculated first. Then the average RMSE for each 5-min group can be calculated.

A quality control is performed for each 5-min group and each component as well as overall 3D position results in order to remove large positioning outliers. For each 5-min group and each component and 3D position, the total number of PPP solutions is 110 (14 days \times 8 stations – 2 missing solutions) and 109 (14 days \times 8 stations – 3 missing solutions) for period 1 and period 2, respectively. After the calculation of average RMSE for each 5-min group and each component as well as 3D position, the positioning RMSE of each set of GNSS PPP solution is compared with the average RMSE. If it is larger than three times average RMSE, that set of GNSS PPP solution will be discarded and the average RMSE is recalculated. At the end, we find that the number of outlier data sets is no more than 9 for each 5-min group in each component as well as overall 3D position.

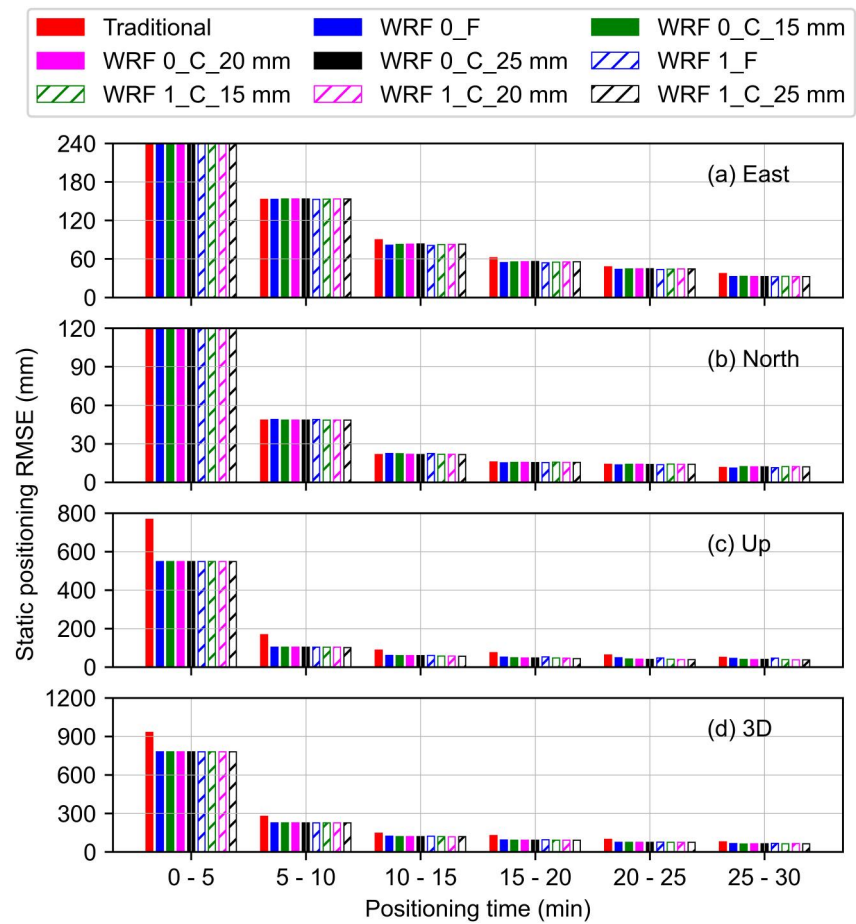


Figure 5. The average positioning RMSE of static PPP corresponding to nine GNSS PPP schemes during period 1 (March 01 to 14, 2020) in the (a) east component, (b) north component, (c) up component, and (d) overall 3D for six 5-min positioning groups within the first 30 min of positioning time.

The average positioning RMSE of static PPP for each 5-min positioning group for period 1 and period 2 are shown in Figures 5 and 6, respectively. In the up component, compared with traditional static PPP, all WRF-enhanced static PPP (WRF-fixed static PPP schemes and WRF-constrained static PPP schemes) evidently have smaller positioning RMSE within the first 30 min of positioning time for period 1. For period 2, we can find that WRF-enhanced static PPP schemes evidently have a better performance in the up component within the first 15 min. After 15 min, the improvements are not evident. This implies that, under extreme weather conditions, due to limited accuracy of WRF-derived wet delay corrections, WRF-enhanced PPP schemes accelerate the convergence speed at early positioning stage but its helpfulness to PPP convergence degrades quickly. In the east and north components, generally, WRF-enhanced static PPP schemes outperform traditional PPP scheme only slightly in both period 1 and period 2.

However, there is no evident difference in the positioning performance between WRF 0-enhanced PPP schemes and WRF 1-enhanced PPP schemes, although the WRF PWV evaluation results have shown a higher accuracy for WRF 1 (assimilation of GNSS PWV). This may be attributed to the distribution of IGS GNSS PPP stations in this study. A considerable part of GNSS PPP stations, for example, CKSV, TCMS, and TWTF, are located outside the assimilation area. These stations may have difficulty in benefitting from assimilation. Thus they shows no superior performance in the WRF 1-enhanced PPP schemes to WRF 0-enhanced PPP schemes.

The kinematic PPP positioning results for each 5-min group for period 1 and period 2 are shown in Figures 7 and 8, respectively. For period 1, the impact of WRF augmentation on the positioning results of the up component degrades rapidly. After using WRF wet delay corrections, we can observe an evident positioning improvement in the up component within the first 5 min but a slightly lower positioning accuracy from 5 to 15 min. After 15 min,

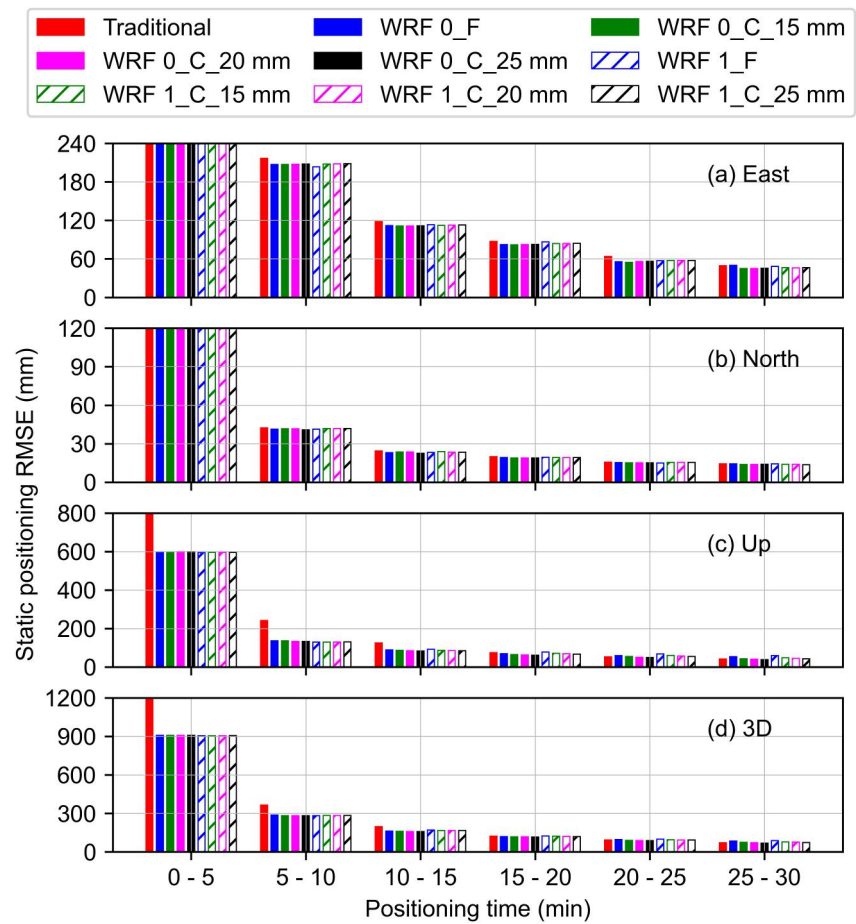


Figure 6. The average positioning RMSE of static PPP corresponding to nine GNSS PPP schemes for period 2 (June 02 to 15, 2020) in the (a) east component, (b) north component, (c) up component, and (d) overall 3D for six 5-min positioning groups within the first 30 min of positioning time.

WRF-enhanced PPP schemes have a slightly smaller positioning RMSE. For period 2, WRF-enhanced PPP schemes show smaller positioning errors in the up component within the first 10 min than the traditional PPP scheme. After 10 min of positioning time, WRF-enhanced PPP schemes even get a larger positioning error. This could be explained as follow. With the increase of positioning time, traditional PPP scheme can estimate the wet delay parameter more accurately. When the estimated wet delay is more accurate than the WRF-derived wet delay, WRF-enhanced PPP schemes may get a poorer positioning performance than traditional PPP. In addition, compared with static mode, the estimation of coordinate parameters in kinematic mode is more sensitive to the observations. This implies that the positioning results in kinematic mode is more easy to be affected by the relatively lower quality WRF-wet delay after 10 min of positioning time. It also should be noted that, in period 2, water vapor condition is active and more difficult to be predicted accurately. WRF Wet delay corrections are only effective for the first 10 min of positioning time, while WRF-enhanced kinematic PPP schemes still show slight improvement at the positioning time of 15–25 min in period 1.

For positioning results in the east, north components, and overall 3D, we can find all the WRF-enhanced PPP schemes generally show a better accuracy than the traditional PPP for both period 1 and period 2.

5.2. Final Positioning Accuracy

The final positioning RMSE statistics corresponding to the static and kinematic PPP results of the last three hours (3 hr UTC to 6 hr UTC) of each day for different PPP schemes are conducted in this section. To perform quality control, based on 3 σ rule, positioning errors larger than the threshold values set in Table 2 are not used in the statistics. A relaxed positioning error threshold is set for period 2 considering high level of water vapor during the

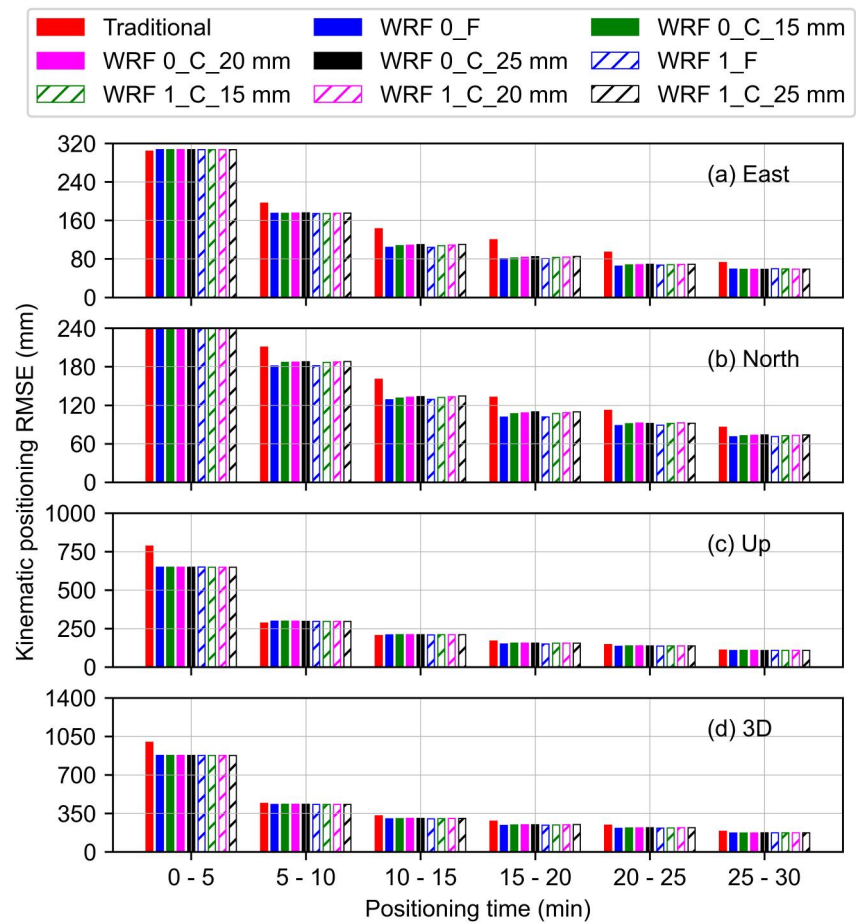


Figure 7. The average positioning RMSE of kinematic PPP corresponding to nine GNSS PPP schemes for period 1 (March 01 to 14, 2020) in the (a) east component, (b) north component, (c) up component, and (d) overall 3D for six 5-min positioning groups within the first 30 min of positioning time.

flooding weather condition in that period has a larger impact on GNSS PPP. “WRF 1_F” scheme has 12 outliers for 3D final positioning error statistics during period 1. For other final positioning error statistical results, no more than 8 PPP positioning solutions are removed for each component, each PPP mode, and each period.

Table 3 shows the average positioning RMSE of static PPP corresponding to each PPP scheme. For period 1, the average positioning RMSE of traditional static PPP in the east, north, and up components and 3D are 4.9, 2.2, 17.8, and 19.1 mm respectively. For period 2, due to the increased water vapor under the flooding weather conditions, the positioning accuracy is much worse. The average positioning RMSE of traditional static PPP errors for period 2 in the east, north, and up components, and 3D are 12.8, 4.0, 30.6, and 35.7 mm, respectively.

For the up component, WRF-constrained static PPP schemes generally have a better positioning accuracy than the traditional PPP scheme. Specifically, WRF-constrained static PPP schemes reduce positioning RMSE in the up component by 14.6% for period 1, while the corresponding improvements in the up component for period 2 are much larger (up to 33.7%). WRF-fixed static PPP schemes have unsatisfactory performances. WRF-fixed PPP static schemes show a considerable accuracy degradation by up to 19.7% in the up component.

For positioning accuracy in the east component during two periods, WRF-constrained static PPP schemes show 1.6%–8.2% of accuracy degradation compared with traditional static PPP scheme. WRF-fixed static PPP schemes show large accuracy degradations by up to 66.4% in the east component for two periods. In the north component, all the WRF-constrained static PPP schemes show a positioning accuracy similar to that of traditional PPP scheme for both period 1 and period 2, while the WRF-fixed static PPP schemes show 13.6%–35.0% of accuracy

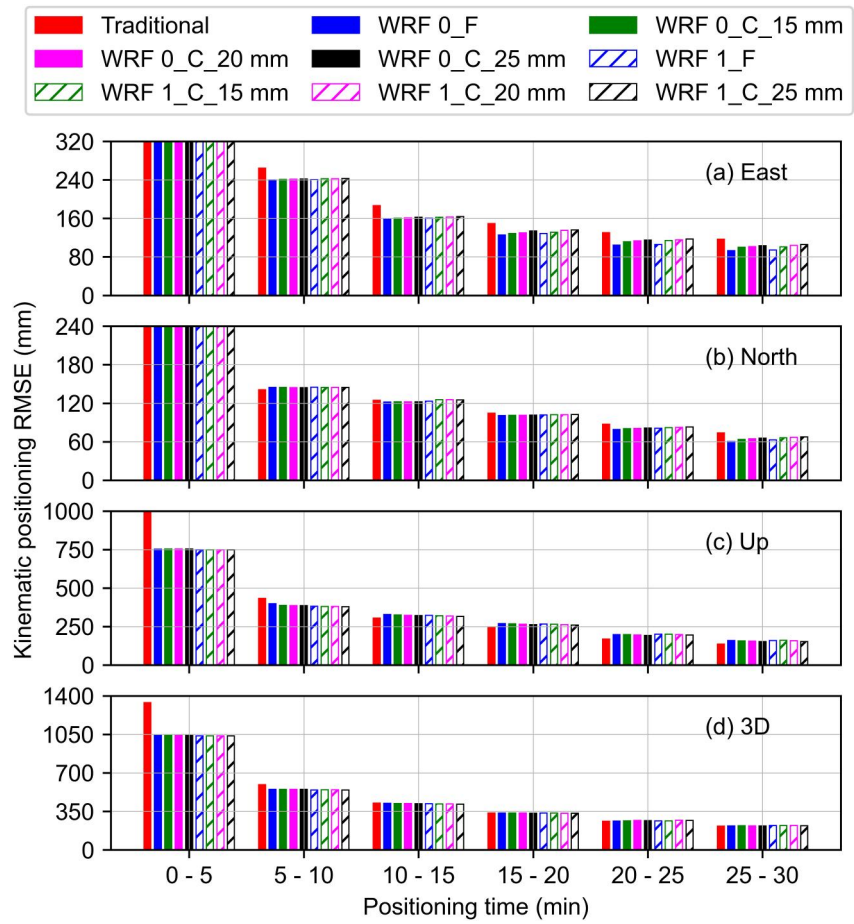


Figure 8. The average positioning RMSE of kinematic PPP corresponding to nine GNSS PPP schemes for period 2 (June 02 to 15, 2020) in the (a) east component, (b) north component, (c) up component, and (d) overall 3D for six 5-min positioning groups within the first 30 min of positioning time.

degradation in the north component for two periods. For the overall 3D positioning results, WRF-constrained static PPP schemes can achieve accuracy improvements of up to 11.5% for period 1 and 22.7% for period 2.

The average positioning RMSE values of kinematic PPP for both period 1 and period 2 are presented in Table 4. We can see that the positioning RMSE of kinematic PPP in period 2 are much larger than those in period 1. This is because of the much larger water vapor variations in period 2. It has been well known water vapor variation is difficult to model and can result in considerable error in GNSS positioning.

In the up component, all the WRF-constrained kinematic PPP schemes show higher positioning accuracy in two periods. The accuracy improvements are ranging from 9.8% to 13.8% for period 1% and 13.9%–19.0% for period

Table 2
The Positioning Error Thresholds Set for East, North, and Up Components and Overall 3D in Final Positioning RMSE Statistics

Experiment period	PPP mode	East (mm)	North (mm)	Up (mm)	3D (mm)
Period 1	Static	20	10	60	60
	Kinematic	30	20	100	110
Period 2	Static	50	20	100	110
	Kinematic	100	60	150	190

Table 3
The Average Positioning RMSE of Static PPP in the East, North, and Up Components and Overall 3D

Period	Schemes	East (mm)	North (mm)	Up (mm)	3D (mm)
Period 1	Traditional	4.9	2.2	17.8	19.1
	WRF 0_F	7.5 (53.1%)	2.5 (13.6%)	21.3 (19.7%)	23.2 (21.5%)
	WRF 0_C_15 mm	5.2 (6.1%)	2.2 (0.0%)	15.7 (−11.8%)	17.3 (−9.4%)
	WRF 0_C_20 mm	5.1 (4.1%)	2.2 (0.0%)	16.1 (−9.6%)	17.6 (−7.9%)
	WRF 0_C_25 mm	5.0 (2.0%)	2.2 (0.0%)	16.5 (−7.3%)	17.9 (−6.3%)
	WRF 1_F	7.9 (61.2%)	2.5 (13.6%)	20.3 (14.0%)	21.5 (12.6%)
	WRF 1_C_15 mm	5.3 (8.2%)	2.2 (0.0%)	15.2 (−14.6%)	16.9 (−11.5%)
	WRF 1_C_20 mm	5.2 (6.1%)	2.2 (0.0%)	15.8 (−11.2%)	17.3 (−9.4%)
Period 2	Traditional	12.8	4.0	30.6	35.7
	WRF 0_F	21.3 (66.4%)	5.3 (32.5%)	35.9 (17.3%)	45.0 (26.1%)
	WRF 0_C_15 mm	13.6 (6.2%)	4.1 (2.5%)	20.3 (−33.7%)	27.6 (−22.7%)
	WRF 0_C_20 mm	13.4 (4.7%)	4.1 (2.5%)	22.5 (−26.5%)	29.0 (−18.8%)
	WRF 0_C_25 mm	13.1 (2.3%)	4.1 (2.5%)	24.4 (−20.3%)	30.4 (−14.8%)
	WRF 1_F	21.2 (65.6%)	5.4 (35.0%)	36.1 (18.0%)	45.2 (26.6%)
	WRF 1_C_15 mm	13.3 (3.9%)	4.1 (2.5%)	21.4 (−30.1%)	28.4 (−20.4%)
	WRF 1_C_20 mm	13.2 (3.1%)	4.1 (2.5%)	23.2 (−24.2%)	29.6 (−17.1%)
WRF 1_C_25 mm	13.0 (1.6%)	4.1 (2.5%)	25.0 (−18.3%)	30.9 (−13.4%)	

Note. The positive/negative percentage in the parentheses means the increase/decrease in percentage of positioning RMSE of WRF-enhanced PPP scheme compared with the traditional PPP scheme.

Table 4
The Average Positioning RMSE of Kinematic PPP in the East, North, and Up Components and Overall 3D

Period	Schemes	East (mm)	North (mm)	Up (mm)	3D (mm)
Period 1	Traditional	9.3	6.8	32.7	35.0
	WRF 0_F	10.3 (10.8%)	7.0 (2.9%)	30.2 (−7.6%)	33.2 (−5.1%)
	WRF 0_C_15 mm	9.6 (3.2%)	6.6 (−2.9%)	28.2 (−13.8%)	30.9 (−11.7%)
	WRF 0_C_20 mm	9.4 (1.1%)	6.6 (−2.9%)	28.9 (−11.6%)	31.4 (−10.3%)
	WRF 0_C_25 mm	9.4 (1.1%)	6.6 (−2.9%)	29.5 (−9.8%)	32.0 (−8.6%)
	WRF 1_F	10.8 (16.1%)	7.2 (5.9%)	31.8 (−2.8%)	34.9 (−0.3%)
	WRF 1_C_15 mm	9.7 (4.3%)	6.6 (−2.9%)	28.4 (−13.1%)	31.2 (−10.9%)
	WRF 1_C_20 mm	9.6 (3.2%)	6.6 (−2.9%)	29.0 (−11.3%)	31.6 (−9.7%)
Period 2	Traditional	23.9	15.1	56.9	65.3
	WRF 0_F	30.7 (28.5%)	22.9 (51.7%)	53.1 (−6.7%)	68.3 (4.6%)
	WRF 0_C_15 mm	27.0 (13.0%)	18.2 (20.5%)	46.1 (−19.0%)	58.8 (−10.0%)
	WRF 0_C_20 mm	26.0 (8.8%)	17.1 (13.2%)	47.0 (−17.4%)	58.7 (−10.1%)
	WRF 0_C_25 mm	25.4 (6.3%)	16.4 (8.6%)	48.6 (−14.6%)	59.4 (−9.0%)
	WRF 1_F	30.7 (28.5%)	22.5 (49.0%)	53.9 (−5.3%)	69.0 (5.7%)
	WRF 1_C_15 mm	26.7 (11.7%)	18.0 (19.2%)	46.8 (−17.8%)	59.3 (−9.2%)
	WRF 1_C_20 mm	25.8 (7.9%)	16.9 (11.9%)	47.6 (−16.3%)	59.2 (−9.3%)
WRF 1_C_25 mm	25.3 (5.9%)	16.3 (7.9%)	49.0 (−13.9%)	59.9 (−8.3%)	

Note. The positive/negative percentage in the parentheses means the increase/decrease in percentage of positioning RMSE of WRF-enhanced PPP schemes compared with the traditional PPP scheme.

Table 5

The Average Convergence Time of Nine GNSS Static PPP Schemes in the East, North, and Up Components, for Period 1 (March 01 to 14, 2020) and Period 2 (June 02 to 15, 2020)

Period	Schemes	East (min)	North (min)	Up (min)
Period 1	Traditional	14.6	3.8	11.0
	WRF 0_F	14.5 (−0.7%)	3.7 (−2.6%)	6.4 (−41.8%)
	WRF 0_C_15 mm	15.1 (3.4%)	3.7 (−2.6%)	6.7 (−39.1%)
	WRF 0_C_20 mm	15.0 (2.7%)	3.7 (−2.6%)	7.0 (−36.4%)
	WRF 0_C_25 mm	15.0 (2.7%)	3.7 (−2.6%)	7.1 (−35.5%)
	WRF 1_F	15.1 (3.4%)	3.7 (−2.6%)	6.5 (−40.9%)
	WRF 1_C_15 mm	15.1 (3.4%)	3.7 (−2.6%)	6.8 (−38.2%)
	WRF 1_C_20 mm	15.2 (4.1%)	3.7 (−2.6%)	6.9 (−37.3%)
	WRF 1_C_25 mm	15.1 (3.4%)	3.7 (−2.6%)	7.1 (−35.5%)
Period 2	Traditional	16.8	3.4	11.2
	WRF 0_F	15.4 (−8.3%)	3.2 (−5.9%)	9.1 (−18.7%)
	WRF 0_C_15 mm	15.6 (−7.1%)	3.2 (−5.9%)	8.6 (−23.3%)
	WRF 0_C_20 mm	15.5 (−7.7%)	3.2 (−5.9%)	8.4 (−25.0%)
	WRF 0_C_25 mm	15.6 (−7.1%)	3.2 (−5.9%)	8.4 (−25.0%)
	WRF 1_F	16.1 (−4.2%)	3.2 (−5.9%)	9.0 (−19.6%)
	WRF 1_C_15 mm	16.1 (−4.2%)	3.2 (−5.9%)	8.4 (−25.0%)
	WRF 1_C_20 mm	16.2 (−3.6%)	3.2 (−5.9%)	8.4 (−25.0%)
	WRF 1_C_25 mm	16.1 (−4.2%)	3.2 (−5.9%)	8.4 (−25.0%)

Note. The negative (positive) percentages are the amount of reduction (increase) percentages of convergence time for the WRF-enhanced PPP schemes compared to the traditional PPP scheme. PPP solutions with convergence time longer than 1 hour are not considered in the statistics.

2. WRF-fixed kinematic PPP schemes improve positioning accuracy for up component by up to 7.6% and 6.7% for period 1 and period 2, respectively.

For the east component, all the WRF-enhanced kinematic PPP schemes have larger positioning RMSE than traditional PPP in both periods. Particularly for period 2, WRF-fixed kinematic PPP schemes degrade positioning accuracy in the east component by 28.5%. For the north component, WRF-enhanced kinematic PPP schemes generally have a performance similar to traditional PPP scheme for period 1, while considerable accuracy degradation is found in period 2, particularly for WRF-fixed kinematic PPP. The accuracy degradations in the north component for the WRF-fixed kinematic PPP schemes are 49.0%–51.7% for period 2.

5.3. Convergence Time

The convergence time of all GNSS PPP schemes is analyzed. In this study, we regard the last epoch with a positioning error larger than the threshold value given for each component as the convergence time for that corresponding component. For both static and kinematic modes, the positioning error thresholds used in convergence statistics for the east, north, and up components are set to 0.1, 0.1, and 0.15 m, respectively. For static or kinematic PPP mode, there are totally 110 and 109 PPP solutions in each PPP scheme for period 1 and period 2, respectively. Those PPP solutions whose convergence time exceed 1 hour are regarded as un-converged solutions and will be discarded in the statistics of final convergence time.

Table 5 shows the average convergence time of static PPP for period 1 and period 2. It should be noted that there are no more than 2 un-converged PPP solutions for the up component for each static PPP scheme in each period. For the east component, there are 1–5 of un-converged PPP solutions for each PPP scheme in each period. All static PPP solutions can achieve convergence in the north component within 1 hr. Enhanced by WRF-derived wet delay corrections, significant convergence improvements can be found in the up

component for both period 1 and period 2. Specifically, in the up component, WRF-enhanced static PPP schemes reduce the convergence time by 35.5%–41.8% for period 1, while the convergence improvements for period 2 range from 18.7% to 25.0%. Almost all WRF-enhanced static PPP schemes show a slightly longer convergence time in east component for period 1, while WRF-enhanced PPP schemes show 3.6%–8.3% of convergence time reductions for in east component for period 2. For the north component, WRF-enhanced static PPP schemes improve the convergence speed by 2.6% and 5.9% for period 1 and period 2, respectively.

The average kinematic PPP convergence time for period 1 and period 2 are shown in Table 6. For period 1, all WRF-enhanced PPP schemes have a shorter convergence time in all components. Specifically, the convergence time reductions in the east, north, and up components are 10.3%–13.6%, 9.0%–13.5%, and 5.2%–8.2%, respectively. It should be noted that, for the up component, WRF 1_F (fixed by wet delay corrections from WRF scheme 1) has 16 un-converged PPP solutions, while the number of un-converged solutions for other GNSS PPP schemes are ranging from 8 to 13. In the east component, there are 17 un-converged PPP solutions for the traditional PPP scheme and 12 to 14 un-converged solutions for the WRF-enhanced PPP schemes. In the north component, there are only 3 un-converged PPP solutions for each GNSS PPP scheme.

For period 2, all the WRF-enhanced PPP schemes have a longer convergence time (5.1%–13.6% of increase in convergence time) than the traditional PPP scheme in the up component, while all the WRF-enhanced PPP schemes show convergence time reductions by 4.4%–13.5% in the east component and 4.0%–8.5% in the north component. However, it should be noted that WRF-constrained kinematic PPP schemes have more converged PPP solutions in the up component for period 2, which implies a more robust positioning performance in the up component. Due to the highly variable water vapor condition during period 2, there are much more un-converged PPP solutions in each component for period 2. Specifically, in the up component, there are 35 un-converged PPP solutions for the traditional PPP scheme, 38 to 39 un-converged solutions for the WRF-fixed PPP schemes, and 27

Table 6
The Average Convergence Time of Nine GNSS Kinematic PPP Schemes in the East, North, and Up Components, for Period 1 (March 01 to 14, 2020) and Period 2 (June 02 to 15, 2020)

Period	Schemes	East (min)	North (min)	Up (min)
Period 1	Traditional	21.3	22.3	19.4
	WRF 0_F	18.4 (−13.6%)	19.4 (−13.0%)	18.3 (−5.7%)
	WRF 0_C_15 mm	18.7 (−12.2%)	19.6 (−12.1%)	18.3 (−5.7%)
	WRF 0_C_20 mm	18.9 (−11.3%)	19.9 (−10.8%)	18.3 (−5.7%)
	WRF 0_C_25 mm	19.0 (−10.8%)	20.2 (−9.4%)	18.3 (−5.7%)
	WRF 1_F	18.5 (−13.1%)	19.3 (−13.5%)	18.4 (−5.2%)
	WRF 1_C_15 mm	18.5 (−13.1%)	19.7 (−11.7%)	17.9 (−7.7%)
	WRF 1_C_20 mm	19.1 (−10.3%)	19.8 (−11.2%)	17.9 (−7.7%)
Period 2	Traditional	27.5	20.0	25.7
	WRF 0_F	23.8 (−13.5%)	18.3 (−8.5%)	27.0 (5.1%)
	WRF 0_C_15 mm	26.3 (−4.4%)	18.3 (−8.5%)	28.1 (9.3%)
	WRF 0_C_20 mm	26.0 (−5.5%)	18.5 (−7.5%)	28.0 (8.9%)
	WRF 0_C_25 mm	26.2 (−4.7%)	18.7 (−6.5%)	28.2 (9.7%)
	WRF 1_F	25.3 (−8.0%)	19.1 (−4.5%)	27.3 (6.2%)
	WRF 1_C_15 mm	25.7 (−6.5%)	19.1 (−4.5%)	29.2 (13.6%)
	WRF 1_C_20 mm	25.9 (−5.8%)	19.1 (−4.5%)	28.5 (10.9%)
	WRF 1_C_25 mm	25.7 (−6.5%)	19.2 (−4.0%)	27.8 (8.2%)

Note. The negative (positive) percentages are the amount of reduction (increase) percentages of convergence time for the WRF-enhanced PPP schemes compared to the traditional PPP scheme. PPP solutions with convergence time longer than 1 hour are not considered in the statistics.

to 28 un-converged PPP solutions for the WRF-constrained PPP solutions. In the east component, 22 to 24 of PPP solutions cannot achieve convergence within 1 hr in the east component for each PPP scheme. In the north component, there are 5–10 un-converged PPP solutions for each scheme.

6. Discussion

In this study, we used WRF-derived wet delay corrections to augment the GNSS PPP positioning performance for two periods with different weather conditions, that is, period 1 (March 01 to 14, 2020, average PWV: 23.5 kg/m²) and period 2 (June 02 to 15, 2020, flooding weather with average PWV: 55.6 kg/m²), in South China. Similar to the previous studies (Cui et al., 2022; Wang & Liu, 2019; Yao et al., 2018), introducing accurate external water vapor data can significantly improve the GNSS PPP performance in terms of positioning accuracy and convergence speed in the up component. Specifically, in this study, WRF-derived wet delay corrections produce a larger augmentation impact on the positioning accuracy for period 2 than that of period 1. For period 1, WRF-enhanced PPP schemes reduce positioning RMSE in the up component by up to 14.6% and 13.8% for static and kinematic modes, respectively. The corresponding improvements in the up component for period 2 are up to 33.7% and 19.0% for static and kinematic PPP modes, respectively. This demonstrates the significance of accurate external water vapor data for GNSS PPP under the severe weather condition when the water vapor condition is very unstable.

Additionally, our study shows that using external water vapor corrections, that is, WRF-derived wet delay corrections, generally does not improve the horizontal positioning accuracy. This is similar to the results shown in Wang and Liu (2019), in which water vapor observations from a collocated Water Vapor Radiometer (WVR) were used to augment GNSS PPP.

Compared with traditional water vapor augmentation data sources, such as collocated water vapor observation systems (Wang & Liu, 2019), regional GNSS network (Cui et al., 2022; Li et al., 2021), empirical tropospheric delay models (Chen & Liu, 2015; Chen et al., 2020; Zhang et al., 2016), and global NWP models (Lu et al., 2017), WRF, as an advanced mesoscale NWP model, has several major advantages in augmenting GNSS PPP, particularly for high precision GNSS real-time PPP:

1. WRF model can forecast water vapor data with a very high spatiotemporal resolution. In this study, we design the WRF model with 5 km of spatial resolution and hourly forecasting temporal resolution. This spatiotemporal resolution can be further improved according to users' demands when enough computational resources are available.
2. WRF model can forecast water vapor data with a high accuracy. As shown in Figure 3, the PWV forecasting RMSE within 24 hr are no more than 2.7 and 3.8 kg/m² for period 1 and period 2, respectively, which are equivalent to around 17.6 and 24.7 mm of RMSE in ZWD. In comparison, empirical wet delay models normally have a poorer performance. Chen and Liu (2015) evaluated the performance of 18 wet delay models in China region using 10 years of radiosonde data. Even for the Baby semiempirical model, which achieved the best agreement with the radiosonde data among the empirical and semiempirical models, the ZWD RMSE was 33.2 mm.

The encouraging results in this study have demonstrated that WRF-enhanced PPP strategies can considerably improve the positioning accuracy in the up component. WRF-enhanced PPP therefore can produce better performance than traditional PPP for various solid earth applications, such as ocean loading displacement estimation (L. Zhang et al., 2021) and plate movement monitoring (Wang & Shen, 2020), in which high-accuracy positioning service is needed.

It is noted that the IGS GNSS stations used in PPP are not evenly distributed in this study. Some of IGS stations, for example, CKSV, TCMS, and TWTF, are far away from the GNSS assimilation stations. These GNSS station may barely benefit from assimilation. This could be one potential reason why the statistical results in this study for PPP schemes augmented by WRF 1 (assimilation of GNSS PWV) does not show a better performance than those PPP schemes augmented by WRF 0 (no assimilation).

7. Conclusions

We have extensively investigated the result of assimilation of GNSS PWV data into WRF model by examining the effectiveness of wet delay from WRF forecasting in GNSS PPP accuracy. GNSS PPP performance with WRF-derived wet delays is tested in two periods that is, period 1 (March 01 to 14, 2020) and period 2 (June 02 to 15, 2020) in South China. Period 1 and period 2 have different weather conditions. Period 2 is under flooding weather condition and has a much higher average PWV (55.6 kg/m²) than period 1 (23.5 kg/m²). Period 2 is selected because we want to see the performance of WRF-enhanced PPP under severe weather conditions. Additionally, in the study, GNSS PWV data from 277 and 263 GNSS stations are assimilated into the WRF model in period 1 and period 2, respectively, to improve the accuracy of wet delay forecasting results.

The positioning results of eight WRF-enhanced PPP schemes are compared with the traditional PPP scheme, several conclusions can be summarized:

1. WRF-enhanced PPP schemes generally have a better positioning accuracy than traditional PPP scheme in the up component in both static and kinematic modes. The positioning accuracy improvements for wet period 2 are larger than that for less wet period 1. Specifically, WRF-enhanced static PPP schemes improve final PPP positioning accuracy in the up component by up to 14.6% and 33.7% for period 1 and period 2, respectively. For kinematic mode, augmented by WRF wet delay corrections, the corresponding positioning accuracy improvements in the up component are up to 13.8% and 19.0% for period 1 and period 2, respectively.
2. The convergence speed of static PPP in the up component is also improved after using wet delay corrections for the two periods. Specifically, for period 1, WRF-enhanced static PPP schemes show a convergence time reduction by up to 35.5%–41.8% in the up component, while the corresponding convergence time reductions for period 2 are up to 18.7%–25.0%. For kinematic mode, WRF-enhanced PPP schemes reduce convergence time in the up component by up to 5.2%–8.2% for period 1. However, for period 2, WRF-enhanced PPP schemes show an increase of up to 5.1%–13.6% in convergence time in the up component.

Data Availability Statement

The Weather Research and Forecasting (WRF) Model (Skamarock et al., 2019) is available at https://www2.mmm.ucar.edu/wrf/users/download/get_source.html. ERA5 data can be downloaded from the Copernicus Climate Change Service (C3S) Climate Data Store (<https://cds.climate.copernicus.eu/#!/search?text=ERA5&type=dataset>) (Hersbach et al., 2023). IGS GNSS raw observations and products used in PPP can be accessed via <https://cddis.nasa.gov/archive/gnss> (Noll, 2010). The Crustal Movement Observation Network Of China (CMONOC) GNSS water vapor data and China Meteorological Administration GNSS Network (CMAGN) water vapor data are available at <https://doi.org/10.5281/zenodo.8036607> (CMONOC & CMA, 2020).

Acknowledgments

The work reported in this paper was partially funded by the Research Grants Council of the Hong Kong Special Administrative Region, China (Project No. PolyU 15221620/B-Q80Q and 15205821/B-Q84W). The authors thank the US National Center for Atmospheric Research (NCAR) for providing WRF model source code. We are grateful for the European Centre for Medium-Range Weather Forecasts (ECMWF) ERA5 data provided by ECMWF. The authors thank GNSS data product service platform of China Earthquake Administration for providing GNSS water vapor data of the Crustal Movement Observation Network Of China (CMONOC). We acknowledge the China Meteorological Administration (CMA) for providing the CMA GNSS Network (CMAGN) water vapor data sets. We thank International GNSS Service (IGS) analysis centers for providing GNSS observations and products used in GNSS precise point positioning.

References

- Askne, J., & Nordius, H. (1987). Estimation of tropospheric delay for microwaves from surface weather data. *Radio Science*, 22(03), 379–386. <https://doi.org/10.1029/RS022i003p00379>
- Barker, D. M., Huang, W., Guo, Y.-R., Bourgeois, A., & Xiao, Q. (2004). A three-dimensional variational data assimilation system for MM5: Implementation and initial results. *Monthly Weather Review*, 132(4), 897–914. [https://doi.org/10.1175/1520-0493\(2004\)132<0897:atvdas>2.0.co;2](https://doi.org/10.1175/1520-0493(2004)132<0897:atvdas>2.0.co;2)
- Bevis, M., Businger, S., Chiswell, S., Herring, T. A., Anthes, R. A., Rocken, C., & Ware, R. H. (1994). GPS meteorology: Mapping zenith wet delays onto precipitable water. *Journal of Applied Meteorology*, 33(3), 379–386. [https://doi.org/10.1175/1520-0450\(1994\)033<0379:gmmzwd>2.0.co;2](https://doi.org/10.1175/1520-0450(1994)033<0379:gmmzwd>2.0.co;2)
- Businger, S., Chiswell, S. R., Bevis, M., Duan, J., Anthes, R. A., Rocken, C., et al. (1996). The promise of GPS in atmospheric monitoring. *Bulletin of the American Meteorological Society*, 77(1), 5–18. [https://doi.org/10.1175/1520-0477\(1996\)077<0005:tpogia>2.0.co;2](https://doi.org/10.1175/1520-0477(1996)077<0005:tpogia>2.0.co;2)
- Chan, P. W., Hon, K. K., Robinson, P., Kosiba, K., Wurman, J., & Li, Q. (2022). Analysis and numerical simulation of a supercell tornado at the Hong Kong adjacent waters. *Meteorological Applications*, 29(2), e2056. <https://doi.org/10.1002/met.2056>
- Chen, B., & Liu, Z. (2015). A comprehensive evaluation and analysis of the performance of multiple tropospheric models in China region. *IEEE Transactions on Geoscience and Remote Sensing*, 54(2), 663–678. <https://doi.org/10.1109/tgrs.2015.2456099>
- Chen, J., Wang, J., Wang, A., Ding, J., & Zhang, Y. (2020). SHAtropE—A regional gridded ZTD model for China and the surrounding areas. *Remote Sensing*, 12(1), 165. <https://doi.org/10.3390/rs12010165>
- CMONOC & CMA. (2020). GNSS PWV data for WRF-enhanced PPP experiment [Dataset]. Zenodo. <https://doi.org/10.5281/zenodo.8036607>
- Cui, B., Wang, J., Li, P., Ge, M., & Schuh, H. (2022). Modeling wide-area tropospheric delay corrections for fast PPP ambiguity resolution. *GPS Solutions*, 26(2), 1–15. <https://doi.org/10.1007/s10291-022-01243-1>
- Davis, J., Herring, T., Shapiro, I., Rogers, A., & Elgered, G. (1985). Geodesy by radio interferometry: Effects of atmospheric modeling errors on estimates of baseline length. *Radio Science*, 20(6), 1593–1607. <https://doi.org/10.1029/RS020i006p01593>
- Dou, F., Lv, X., & Chai, H. (2021). Mitigating atmospheric effects in InSAR stacking based on ensemble forecasting with a numerical weather prediction model. *Remote Sensing*, 13(22), 4670. <https://doi.org/10.3390/rs13224670>
- Dudhia, J. (1996). A multi-layer soil temperature model for MM5. In *Preprints, The sixth PSU/NCAR mesoscale model users' workshop* (pp. 22–24). National Center for Atmospheric Research Boulder, CO.
- Gong, Y., Liu, Z., Chan, P. W., & Hon, K. K. (2021). Augmenting GNSS PPP accuracy in South China using water vapor correction data from WRF assimilation results. In *China satellite navigation conference (CSNC 2021) proceedings* (pp. 653–670). Springer.
- Guo, Y., Wu, Y., Wen, B., Huang, W., Ju, K., Gao, Y., & Li, S. (2020). Floods in China, COVID-19, and climate change. *The Lancet Planetary Health*, 4(10), e443–e444. [https://doi.org/10.1016/s2542-5196\(20\)30203-5](https://doi.org/10.1016/s2542-5196(20)30203-5)
- Hersbach, H., Bell, B., Berrisford, P., Biavati, G., Horányi, A., Muñoz Sabater, J., et al. (2023). ERA5 hourly data on pressure levels from 1940 to present [Dataset]. Copernicus Climate Change Service (C3S) Climate Data Store (CDS). <https://doi.org/10.24381/cds.bd0915c6>
- Hersbach, H., Bell, B., Berrisford, P., Hirahara, S., Horányi, A., Muñoz-Sabater, J., et al. (2020). The ERA5 global reanalysis. *Quarterly Journal of the Royal Meteorological Society*, 146(730), 1999–2049. <https://doi.org/10.1002/qj.3803>
- Hon, K. K. (2020). Tropical cyclone track prediction using a large-area WRF model at the Hong Kong Observatory. *Tropical Cyclone Research and Review*, 9(1), 67–74. <https://doi.org/10.1016/j.tcr.2020.03.002>
- Hong, S.-Y., Noh, Y., & Dudhia, J. (2006). A new vertical diffusion package with an explicit treatment of entrainment processes. *Monthly Weather Review*, 134(9), 2318–2341. <https://doi.org/10.1175/mwr3199.1>
- Hopfield, H. (1969). Two-quartic tropospheric refractivity profile for correcting satellite data. *Journal of Geophysical Research*, 74(18), 4487–4499. <https://doi.org/10.1029/jc074i018p04487>
- Iacono, M. J., Delamere, J. S., Mlawer, E. J., Shephard, M. W., Clough, S. A., & Collins, W. D. (2008). Radiative forcing by long-lived greenhouse gases: Calculations with the AER radiative transfer models. *Journal of Geophysical Research*, 113(D13), D13103. <https://doi.org/10.1029/2008jd009944>
- Kain, J. S. (2004). The Kain–Fritsch convective parameterization: An update. *Journal of Applied Meteorology*, 43(1), 170–181. [https://doi.org/10.1175/1520-0450\(2004\)043<0170:tkcpau>2.0.co;2](https://doi.org/10.1175/1520-0450(2004)043<0170:tkcpau>2.0.co;2)
- Kouba, J., & Héroux, P. (2001). Precise point positioning using IGS orbit and clock products. *GPS Solutions*, 5(2), 12–28. <https://doi.org/10.1007/pl00012883>
- Leontiev, A., Rostkier-Edelstein, D., & Reuveni, Y. (2020). On the potential of improving WRF model forecasts by assimilation of high-resolution GPS-derived water-vapor maps augmented with METEOSAT-11 data. *Remote Sensing*, 13(1), 96. <https://doi.org/10.3390/rs13010096>
- Li, X., Huang, J., Li, X., Lyu, H., Wang, B., Xiong, Y., & Xie, W. (2021). Multi-constellation GNSS PPP instantaneous ambiguity resolution with precise atmospheric corrections augmentation. *GPS Solutions*, 25(3), 1–13. <https://doi.org/10.1007/s10291-021-01123-0>
- Liang, H., Cao, Y., Wan, X., Xu, Z., Wang, H., & Hu, H. (2015). Meteorological applications of precipitable water vapor measurements retrieved by the national GNSS network of China. *Geodesy and Geodynamics*, 6(2), 135–142. <https://doi.org/10.1016/j.geog.2015.03.001>
- Lim, K.-S. S., & Hong, S.-Y. (2010). Development of an effective double-moment cloud microphysics scheme with prognostic cloud condensation nuclei (CCN) for weather and climate models. *Monthly Weather Review*, 138(5), 1587–1612. <https://doi.org/10.1175/2009mwr2968.1>
- Lu, C., Li, X., Zus, F., Heinkelmann, R., Dick, G., Ge, M., et al. (2017). Improving BeiDou real-time precise point positioning with numerical weather models. *Journal of Geodesy*, 91(9), 1019–1029. <https://doi.org/10.1007/s00190-017-1005-2>

- Mateus, P., & Miranda, P. (2022). Using InSAR data to improve the water vapor distribution downstream of the core of the South American low-level jet. *Journal of Geophysical Research: Atmospheres*, 127(7), e2021JD036111. <https://doi.org/10.1029/2021jd036111>
- Mateus, P., Miranda, P., Nico, G., & Catalao, J. (2021). Continuous multitrack assimilation of Sentinel-1 precipitable water vapor maps for numerical weather prediction: How far can we go with current InSAR data? *Journal of Geophysical Research: Atmospheres*, 126(3), e2020JD034171. <https://doi.org/10.1029/2020jd034171>
- Mateus, P., Nico, G., & Catalão, J. (2015). Uncertainty assessment of the estimated atmospheric delay obtained by a numerical weather model (NMW). *IEEE Transactions on Geoscience and Remote Sensing*, 53(12), 6710–6717. <https://doi.org/10.1109/TGRS.2015.2446758>
- Murray, K. D., Bekaert, D. P., & Lohman, R. B. (2019). Tropospheric corrections for InSAR: Statistical assessments and applications to the Central United States and Mexico. *Remote Sensing of Environment*, 232, 111326. <https://doi.org/10.1016/j.rse.2019.111326>
- Noll, C. E. (2010). The crustal dynamics data information system: A resource to support scientific analysis using space geodesy [Dataset]. *Advances in Space Research*, 45(12), 1421–1440. <https://doi.org/10.1016/j.asr.2010.01.018>
- Parrish, D. F., & Derber, J. C. (1992). The National Meteorological Center's spectral statistical-interpolation analysis system. *Monthly Weather Review*, 120(8), 1747–1763. [https://doi.org/10.1175/1520-0493\(1992\)120<1747:tmccs>2.0.co;2](https://doi.org/10.1175/1520-0493(1992)120<1747:tmccs>2.0.co;2)
- Ross, R. J., & Elliott, W. P. (1996). Tropospheric water vapor climatology and trends over North America: 1973–93. *Journal of Climate*, 9(12), 3561–3574. [https://doi.org/10.1175/1520-0442\(1996\)009%3C3561:TWVCAT%3E2.0.CO;2](https://doi.org/10.1175/1520-0442(1996)009%3C3561:TWVCAT%3E2.0.CO;2)
- Rüeger, J. M. (2002). Refractive index formula for radio waves. In *Presented at the FIG XXII Int. Congr., Washington, D.C. USA* (pp. 1–13).
- Saastamoinen, J. (1972). Atmospheric correction for the troposphere and stratosphere in radio ranging satellites. *The Use of Artificial Satellites for Geodesy*, 15, 247–251. <https://doi.org/10.1029/gm015p0247>
- Skamarock, W. C., Klemp, J. B., Dudhia, J., Gill, D. O., Liu, Z., Berner, J., et al. (2019). A description of the advanced research WRF model version 4 [Software]. NCAR Tech Note NCAR/TN-556+STR, 145. <https://doi.org/10.5065/1dfh-6p97>
- Tétreault, P., Kouba, J., Héroux, P., & Legree, P. (2005). CSRS-PPP: An internet service for GPS user access to the Canadian Spatial Reference Frame. *Geomatica*, 59(1), 17–28.
- Vaclavovic, P., Dousa, J., Elias, M., & Kostelecky, J. (2017). Using external tropospheric corrections to improve GNSS positioning of hot-air balloon. *GPS Solutions*, 21(4), 1479–1489. <https://doi.org/10.1007/s10291-017-0628-3>
- Wang, J., & Liu, Z. (2019). Improving GNSS PPP accuracy through WVR PWV augmentation. *Journal of Geodesy*, 93(9), 1685–1705. <https://doi.org/10.1007/s00190-019-01278-2>
- Wang, M., & Shen, Z.-K. (2020). Present-day crustal deformation of continental China derived from GPS and its tectonic implications. *Journal of Geophysical Research: Solid Earth*, 125(2), e2019JB018774. <https://doi.org/10.1029/2019JB018774>
- Wang, X., Zeng, Q., Jiao, J., & Hao, Z. (2021). Evaluation of weather research and forecast (WRF) microphysics schemes in simulating zenith total delay for InSAR atmospheric correction. *International Journal of Remote Sensing*, 42(9), 3456–3473. <https://doi.org/10.1080/01431161.2020.1807649>
- Webb, T., Wadge, G., & Pascal, K. (2020). Mapping water vapour variability over a mountainous tropical island using InSAR and an atmospheric model for geodetic observations. *Remote Sensing of Environment*, 237, 111560. <https://doi.org/10.1016/j.rse.2019.111560>
- Wilgan, K., Hadas, T., Hordyniec, P., & Bosy, J. (2017). Real-time precise point positioning augmented with high-resolution numerical weather prediction model. *GPS Solutions*, 21(3), 1341–1353. <https://doi.org/10.1007/s10291-017-0617-6>
- Xiong, Z., Sang, J., Sun, X., Zhang, B., & Li, J. (2020). Comparisons of performance using data assimilation and data fusion approaches in acquiring precipitable water vapor: A case study of a Western United States of America area. *Water*, 12(10), 2943. <https://doi.org/10.3390/w12102943>
- Yao, Y., Xu, X., Xu, C., Peng, W., & Wan, Y. (2018). GGOS tropospheric delay forecast product performance evaluation and its application in real-time PPP. *Journal of Atmospheric and Solar-Terrestrial Physics*, 175, 1–17. <https://doi.org/10.1016/j.jastp.2018.05.002>
- Zhang, H., Yuan, Y., Li, W., Li, Y., & Chai, Y. (2016). Assessment of three tropospheric delay models (IGGTrop, EGNOS and UNB3m) based on precise point positioning in the Chinese region. *Sensors*, 16(1), 122. <https://doi.org/10.3390/s16010122>
- Zhang, L., Tang, H., & Sun, W. (2021). Comparison of GRACE and GNSS seasonal load displacements considering regional averages and discrete points. *Journal of Geophysical Research: Solid Earth*, 126(8), e2021JB021775. <https://doi.org/10.1029/2021JB021775>
- Zhou, F., Cao, X., Ge, Y., & Li, W. (2020). Assessment of the positioning performance and tropospheric delay retrieval with precise point positioning using products from different analysis centers. *GPS Solutions*, 24(1), 1–11. <https://doi.org/10.1007/s10291-019-0925-0>
- Zumberge, J., Heflin, M., Jefferson, D., Watkins, M., & Webb, F. (1997). Precise point positioning for the efficient and robust analysis of GPS data from large networks. *Journal of Geophysical Research*, 102(B3), 5005–5017. <https://doi.org/10.1029/96JB03860>